Large strain flow curve characterization considering strain rate and thermal effect for 5182-O aluminum alloy

Hongchun Shang[1] · Chong Zhang[1] · Songchen Wang[1] · Yanshan Lou[1]

Abstract

This research aims to characterize the effect of strain rate and temperature on flow behaviours under large plastic deformation for 5182-O aluminum alloy. Experiments are conducted with both dogbone and notched specimens at different strain rates and temperatures. All tests are analyzed by inverse engineering to identify the strain hardening behaviour at large plastic strains up to fracture. The experimental results show the highly coupling effect of strain rate and temperature. The two hardening laws of Swift-Voce model and p-model are calibrated by the finite element model update procedure, and the combination with the smallest error is selected as the input set of the artificial neural network (ANN) model. Then the dynamic hardening behaviours are modelled by the ANN to consider the highly coupled effect. The calibrated ANN model is further applied to ABAQUS/Explicit for numerical simulation under different loading conditions. Taking the finite element calculation time and prediction accuracy into consideration, the ANN model with single hidden layer optimized by particle swarm optimization algorithm is finally selected. The calibration results of the selected ANN model have the best consistency with an acceptable level of numerical computation time.

Introduction

Aluminum alloys are considered to be the most ideal lightweight materials to replace advanced high-strength steels to improve energy efficiency [1]. The widespread application of Al-Mg alloys (5xxx series) is due to their high specific strength, good corrosion resistance and recycling potential. However, moderate strength and dynamic strain aging (DSA) result in lower formability of Al-Mg alloys compared to highly formable steel sheets [2]. The DSA effect is essentially caused by the interaction between solute atoms and dislocations [3]. Negative strain rate sensitivity only occurs within a certain temperature and strain rate range due to the diffusion motion of solute atoms. High temperature [4] and high speed [5] forming technology is applied to improve sheet forming ability to overcome these limitations. Many

studies have reported that the 5182-O aluminum alloy is negative strain rate sensitivity at room temperature, while the strain rate sensitivity becomes positive with increasing temperature [6, 7]. The complex strain rate sensitive behavior of 5182-O aluminum alloy at different temperature and strain rate ranges is considered to be the greatest challenge in modeling the observed stress-strain response [8]. Therefore, reliable and safe characterization of post-necking material behavior is crucial to improve the prediction accuracy of finite element (FE) simulations [9].

The accurate description of the hardening characteristics of the sheet metal is the theoretical basis for the FE simulation of the high temperature and high speed forming process, and it is also the key to rationally optimizing the process parameters. The most common method to obtain the hardening curve is to theoretically calculate the experimental data of the uniform deformation before necking from uniaxial tension, but the strain obtained in this way is usually lower than the effective result in the forming process especially at high temperature. Therefore, it is meaningful to properly identify the hardening information of materials at large deformation. There are two approaches to describe large deformation up to fracture according to the effect of

✉ Yanshan Lou
ys.lou@xjtu.edu.cn

1 School of Mechanical Engineering, Xi'an Jiaotong University, 28 Xianning West Road, 710049 Xi'an, Shaanxi, China

loading conditions on the hardening behavior: (a) different types of experiments were introduced to overcome the limitations of uniaxial tension, such as the biaxial tensile tests, shear tests, and multi-layered upsetting tests [10–12], and (b) advanced constitutive model combined with effective data analysis method can extract the hardening characteristics of uniaxial tensile test after necking [13–15]. The shear test has the advantage of inducing high plastic strains due to the approximately zero hydrostatic pressure and plane strain states. Traphöner et al. [11] introduced a new specimen with a specially shaped groove and a new incremental method, which enables very high strains for ductile materials.

The post-necking behavior of plastic materials is usually derived from the pre-necking data measured by conventional experiments and then extrapolated according to the hardening laws. The predicted stress-strain curves of different hardening laws at large strains are very different after necking strain, so this extrapolation method is considered unreliable and potentially unsafe. In the past decade, virtual field method (VFM) and finite element model update (FEMU) are widely utilized to make the simulation results gradually approach the experimental results through iterative optimization [16]. The former is an explicit method based on DIC technique that can accurately measure the full-field strain [17]. The latter is a well-known implicit approach through FE analysis, which makes the experimental results as close as possible to reproduce the hardening behavior after necking in the simulation by continuously adjusting the parameters of the constitutive model. In most studies, the hardening behavior is accurately described by matching post-necking force-displacement data, especially for fracture prediction. Peirs et al. [18] proposed a method involving the identification of constitutive model parameters for FE simulation and extraction of hardening behavior. Mechanical behaviors related to strain rate and temperature are extracted from the shear and tensile test results. Lou et al. [19] calibrated the Swift-Voce hardening law and pressure coupled Drucker function by inverse engineering to accurately simulate the strength between different stress states from yield to fracture. Denys et al. [20] showed that different from the progressive identification strategy, the global identification strategy can accurately describe the strain hardening behavior after necking. Zhang et al. [21] obtained the experimental full-field strain fields through DIC technology, and inversely identified the strain hardening behavior beyond the maximum uniform strain.

The dynamic response of metallic materials is essential for deformation analysis under different temperatures and strain rates. The phenomenological and physics-based constitutive models are proposed to analytically characterize the coupling effect. However, most traditional constitutive models are difficult to accurately describe the dynamic response at different conditions. Machine learning provides an alternative method to achieve data-driven nonlinear mapping based on the principles of human brain organization. Jenab et al. [22] proved that the feed-forward neural network can accurately predict the rheological behavior of the 5182-O aluminium alloy material in different material directions. In order to consider the significant effect of DSA, Li et al. [23] introduced the effective aging time as an additional state variable into the hardening law of the artificial neural network (ANN) model. The back propagation algorithm based on Bayesian regularization is employed to train the neural network and then it is used to describe the stress-strain response associated with the temperature and strain rate of polypropylene [24]. The above results show that the machine learning method can be trained by experimental data and then establish the nonlinear mapping relationship from strain rate, temperature and plastic strain to the flow stress.

In the present work, the dogbone specimens and notch specimens of 5182-O aluminum alloy are performed to tensile tests in the temperature range of 300 K ~ 523 K and the strain rate range of 0.001/s ~ 1/s. Then the FEMU procedure is used to extract the stress-strain of the notched specimen at large strains. In the process, the calibration errors of the two hardening models are compared, and then the input set of the ANN model is determined according to the calibration errors. The trained ANN model predicts the large strain behavior of the notched specimen at different conditions. The ANN model is implemented into the ABAQUS/Explicit to numerically describe the reaction force of the notched specimen at large strains.

Experiments

The material selected for the experiment is 5182-O aluminium alloy in the form of sheets with a size of 500×500 mm. The sheets were drawn-over-mandrel until the thickness is 1.25 mm and received in a fully annealed state. Two types of specimens are manufactured along the rolling direction using laser cutting with the dimensions shown in Fig. 1. The orthogonal test consisting of six temperatures and four strain rates is carried out to comprehensively consider the strain rate and thermal dependence of the material. The six sets of temperatures are spaced at 50 K intervals. Lou and Huh [25] suggested to perform numerical simulation to ensure that different loading speeds can meet the requirements of corresponding strain rates. Corresponding four strain rates are set to compare the strains obtained from the two specimens. The crosshead speeds are controlled at 1.8, 18, 180 and 900 mm/min, respectively, so that the loading rates of the dogbone specimens could be guaranteed to reach 0.001/s,
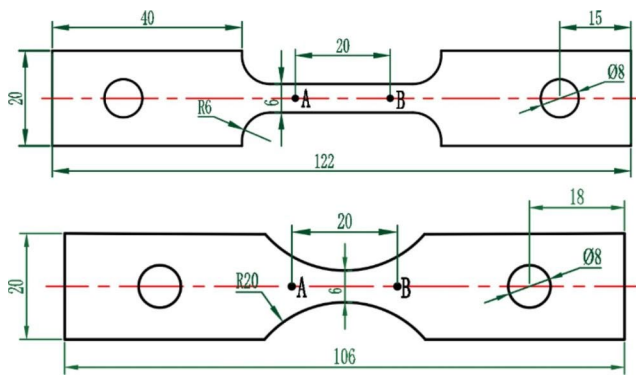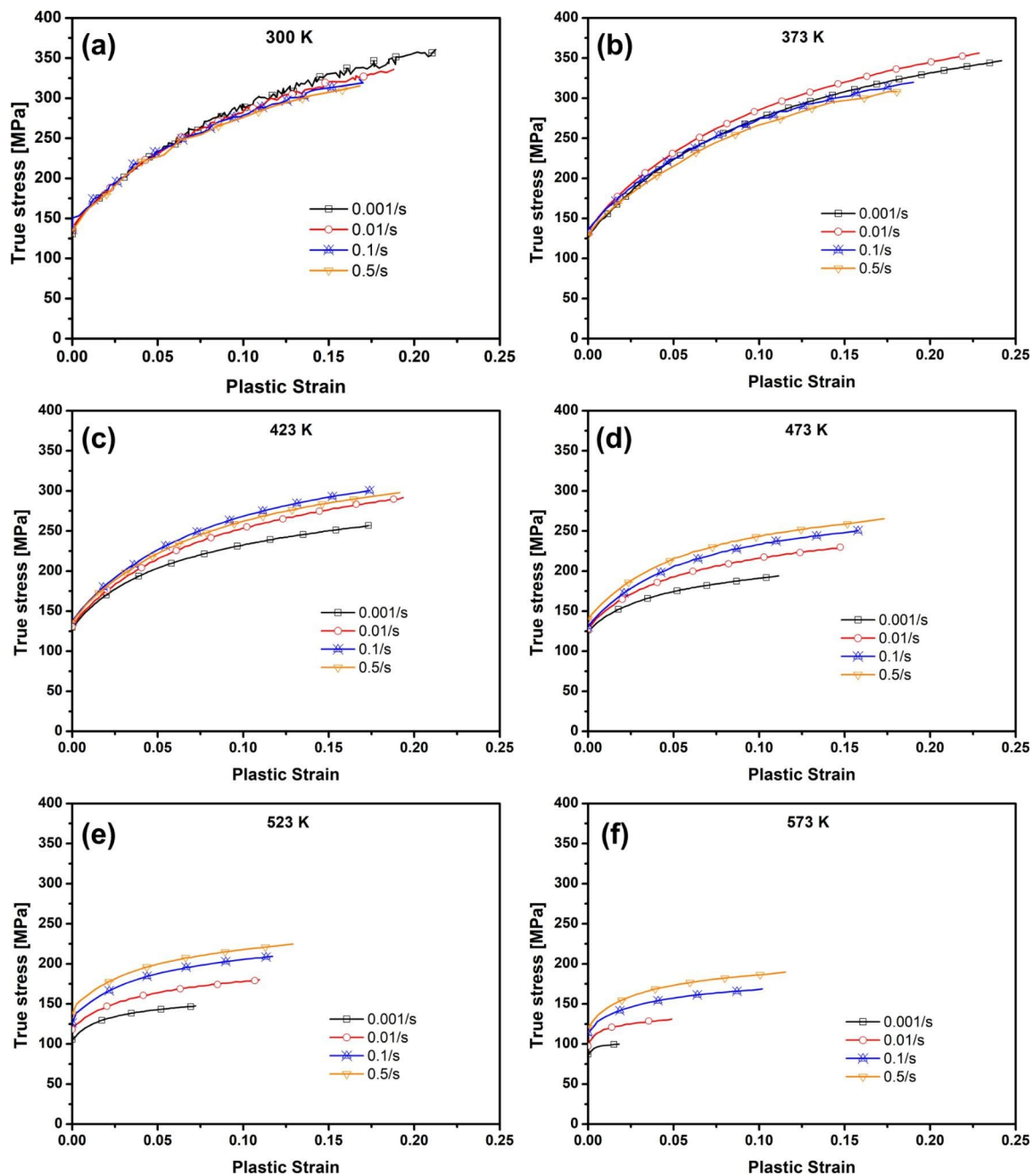
Fig. 1 Dogbone specimen and notched specimen geometries

0.01/s, 0.1/s and 0.5/s. In order to ensure that the notched specimens are stretched at strain rates of 0.001/s, 0.01/s, 0.1/s and 1/s, the crosshead speeds are controlled at 0.9, 9, 90 and 900 mm/min, respectively. Since the dogbone specimen cannot reach the strain rate of 1/s due to the limitation of the experimental equipment, the hardening behavior of the dogbone specimen at 0.5/s is compared with the hardening behavior of the notched specimen at 1/s. At least four repeats are performed for each experimental condition, so a total of 192 experiments are carried out.

The specimen surfaces uniformly covered by the white paint are randomly sprayed with black spots so that the displacement field is captured by the 3D XTOP DIC system. The resolution of the two cameras is 2448×2050 and the acquisition frequency is adjusted according to different loading speeds to ensure that each set of experiments can effectively record 100–200 images during deformation. The force by the load sensor and the stroke by the video extensometer are carried out simultaneously. The distance between points A and B in Fig. 1 represents the initial gauge length for specimens. The heating phase lasts for about 30 min to the target temperature. Then the temperature is kept at the target temperature for about 90 s before starting the test. There could be impact on microstructure especially at high temperature. The effect of microstructure change on flow curves is measured by experimental responses and considered by the constitutive models and ANN prediction implicitly, even though the microstructure effect is not explicitly investigated in this study. The purpose is to achieve the desired temperature as much as possible and make the specimens uniformly heated.

The true stress-plastic strain curves are analytically computed by the force-stroke curves of the dogbone specimens before the maximum force because the deformation is not uniform after necking at the maximum force. The computed flow curves are compared under different conditions of temperature and strain rate in Fig. 2. It is observed that the flow stress at room temperature gradually decreases with the strain rate, indicating that the material exhibits a negative

strain rate sensitivity. Moreover, the effect of the strain rate on the flow stress in the test range is different at 373 and 423 K. The flow stress at 0.01/s obviously exceeds the other three strain rates at 373 K. The flow stress becomes the highest for 423 K at a strain rate of 0.1/s, and its strength is 1.17 times that at a strain rate of 0.001/s. The comparison of results shows that the positive strain rate influence gradually increases with the temperature. The strain rate strengthening effect is significant up to 473 K. In addition, the difference in flow stress between the four sets of strain rates gradually becomes larger as the temperature increases. The above experimental results show that the effects of temperature and strain rate on flow stress are nonlinearly coupled. Numerous studies have shown that the negative strain rate sensitivity is due to the effect of DSA, which is essentially the result of the interaction of moving dislocations and diffusing solute atoms [26]. Fewer vacancies are created during stretching at low strain rates, so it takes longer for solute atoms to diffuse into moving dislocations than at high strain rates. Because the prolonged aging time causes more solute atoms to diffuse around the dislocation, the interaction force between the dislocation and the diffusing solute atoms increases. The higher interaction force at low strain rate results from the diffusion of more solute atoms around the dislocation due to the prolonged aging time [27]. In addition to the negative strain rate sensitivity, another characteristic feature of the DSA effect is that the tensile curve is no longer smooth but some types of serrations appear. The large C-type serrations appear in the latter part of the plastic deformation. The different serration types appear on the stress-strain curves only when the pinning effect of the solute atomic gas on the dislocation is large enough [28]. Experimental results with dogbone specimens are used to analytically compute the flow curves when the deformation is uniform at the gauge before the maximum force. However, the flow curves cannot be analytically computed when the deformation is localized after necking especially at high temperature. In this study, the experimental force-stroke curves of notched specimens in Fig. 1 is adopted to characterize the strain hardening behaviour up to large strain after necking by the inverse engineering approach [19]. In the inverse engineering approach, the flow curve is optimized so that the numerical predicted force-stroke curve matches with the experimental result with the least difference. The force-stroke curves of dogbone specimens are not suggested to be used in the inverse engineering approach because necking of dogbone specimens is affected both by the material properties and the geometric defects of the gauge during manufacturing of the specimens. But for the notched specimens, material properties are the main reason for the necking in the designed geometric defect of the notched specimens. Therefore, the

Fig. 2 Experimental true stress-plastic strain curves from tensile testing of dogbone specimens at different strain rates and temperatures: (a) 300 K, (b) 373 K, (c) 423 K, (d) 473 K, (e) 523 K and (f) 573 K

repeatability of the notched specimens is much better than that of the dogbone specimens after necking.

In order to specifically reflect strain rate effects on the flow behavior of the investigated materials, the corresponding true stresses are extracted at three representative strain levels for all six temperatures as compared in Fig. 3. In order to cover a large deformation range, the strain values of 0.002, 0.05 and 0.1 are selected for 5182-O aluminum alloy. The necking strain under some conditions is relatively small, so no results are shown in Fig. 3 for the corresponding

extraction strain. For example, the necking strain is only 0.018 at 573 K with a strain rate of 0.001/s, which is much lower than other conditions. Mirone et al. [29] showed that inertial and material rate-dependence delay the necking initiation at high strain rates. There is not enough time for dislocations to annihilate and rearrange at high strain rate. The movement of dislocations is easier due to the temperature softening effect, so the stress at 573 K is lower and necking occurs earlier than at other temperatures. Thus the necking strain observed at 573 K with a strain rate of 0.001/s is the
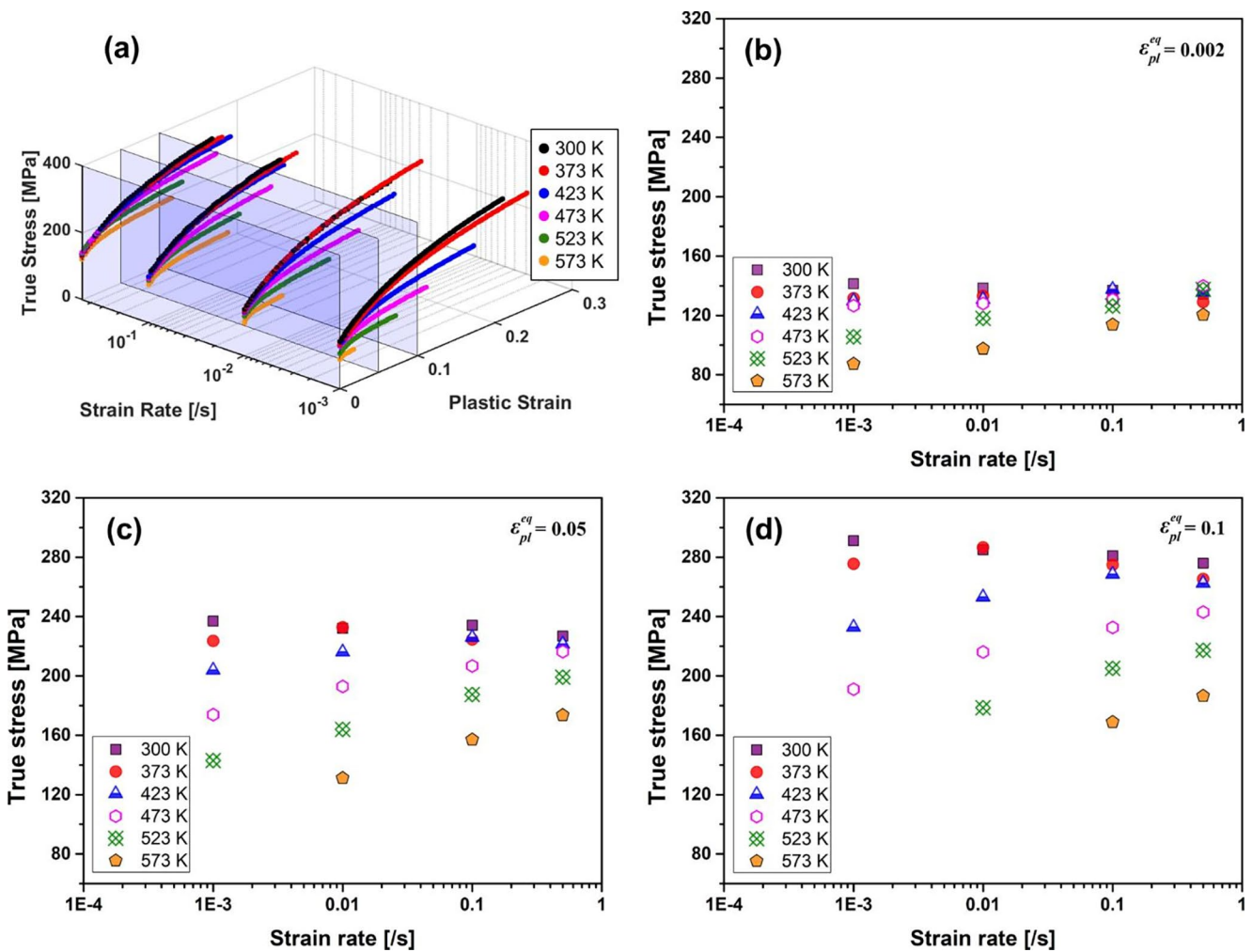
Fig. 3 (a) True stress-plastic strain curves for different temperatures and loading speed; (b), (c) and (d) The distribution of the true stress over strain rate determined from uniaxial tensile tests at different plastic strain levels

lowest compared to all other strain rates. From the comparison of the results in Fig. 3, it can be found that under the same strain, the amplitude of the stress at the six temperatures gradually decreases with the increase of the strain rate. The difference in stress between the different temperatures is the greatest at the strain rate of 0.001/s for the three strain levels. For example, the amplitude of stress in Fig. 3(a) is 54.03 MPa and 19.44 MPa at the strain rate of 0.001/s and 0.5/s, respectively. At the same strain rate, the amplitude of stress at six temperatures also increases gradually with the increase of strain. For the strain rate of 0.1/s, the range of stress increases from 23.75 MPa to 112.06 MPa as the strain increases. It is expanded by 4.72 times through the range of strain indicating that the effect of strain reinforcement is significant. Moreover, the negative strain rate effect can be observed at 300 K. It can be observed that the maximum stress at 373 and 423 K is at strain rate of 0.01/s and 0.1/s, respectively. The stress after 473 K is positively correlated with the logarithm of the strain rate. These observations indicate the significance of the strain rate dependence for the accurate description of the DSA related phenomena.

The experimental results of notched specimens under different conditions are compared in Fig. 4. The specimens necked before failure at room temperature and the necking became more prominent with the increase of temperature. The necking occurs at a displacement of 0.28 but cracks appear until the displacement is 8.43 at 573 K with a strain rate of 0.001/s. The 5182-O alloy is manufactured under annealing conditions, which reduces the strength but the failure strain (total elongation) increases with temperature [30]. The effect of higher temperature is to activate more dislocation mobility, higher dislocation entanglement and greater storage potential to improve ductility. In conclusion, the 5182-O alloy deformed greatly under the coupling effects, and the hardening curves of uniaxial tensile test are limited due to necking. Therefore, the FEMU method should be introduced for uniaxial tensile test to obtain the hardening behavior of 5182-O sheet metal under large
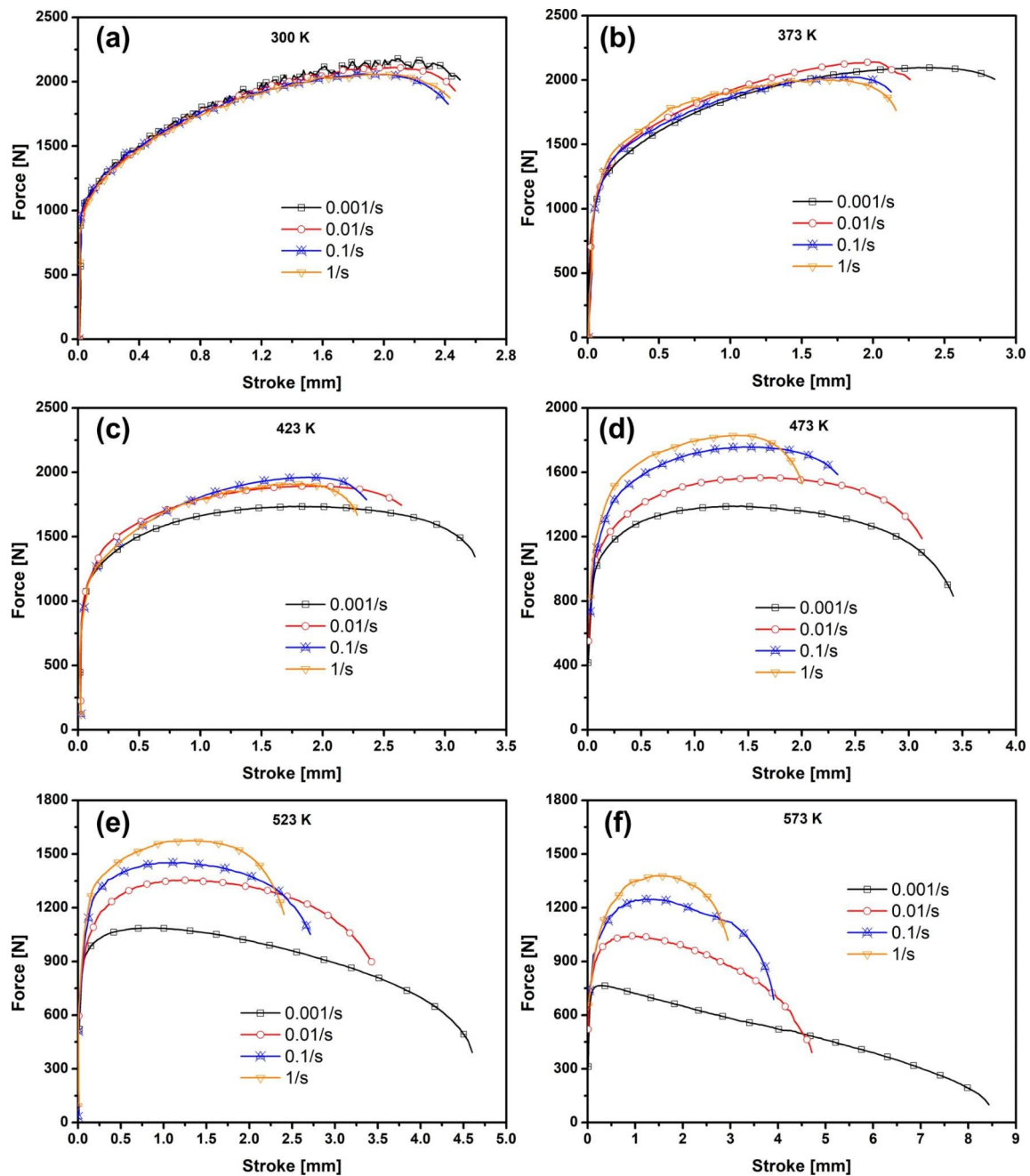
Fig. 4 Experimental force-displacement curves from tensile testing of notched specimens: (a) 300 K, (b) 373 K, (c) 423 K, (d) 473 K, (e) 523 K and (f) 573 K

deformation. Figure 5 shows the effective surface strain fields of the dogbone and notch specimens measured by DIC at maximum force for different strain rates of 573 K. It is clearly observed that the necking strain increases with the strain rate at a high temperature such as 573 K, which indicates that high speed can improve the formability of the material.

Finite element modeling and inverse engineering approach

General frame work

The flowchart in Fig. 6 illustrates the inverse engineering process based on the FEMU method. The basic task is to minimize the difference between the experimental measurements and the numerical calculation results of the FE
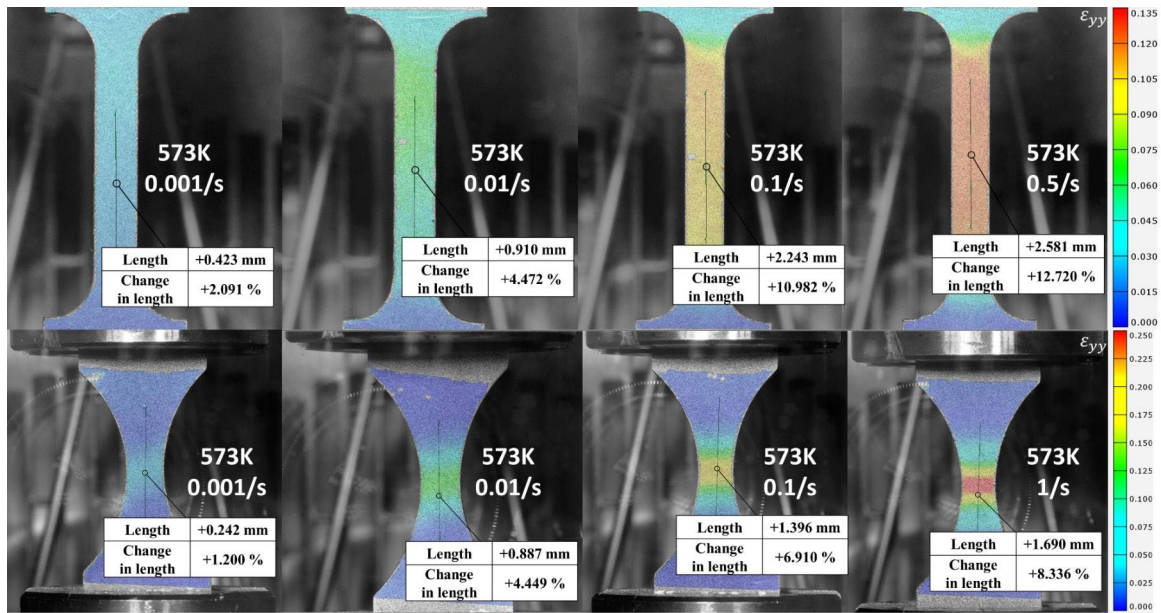
Fig. 5 The effective surface strain fields measured by DIC at the maximum force of the dogbone and notched specimens for different strain rates of 573 K
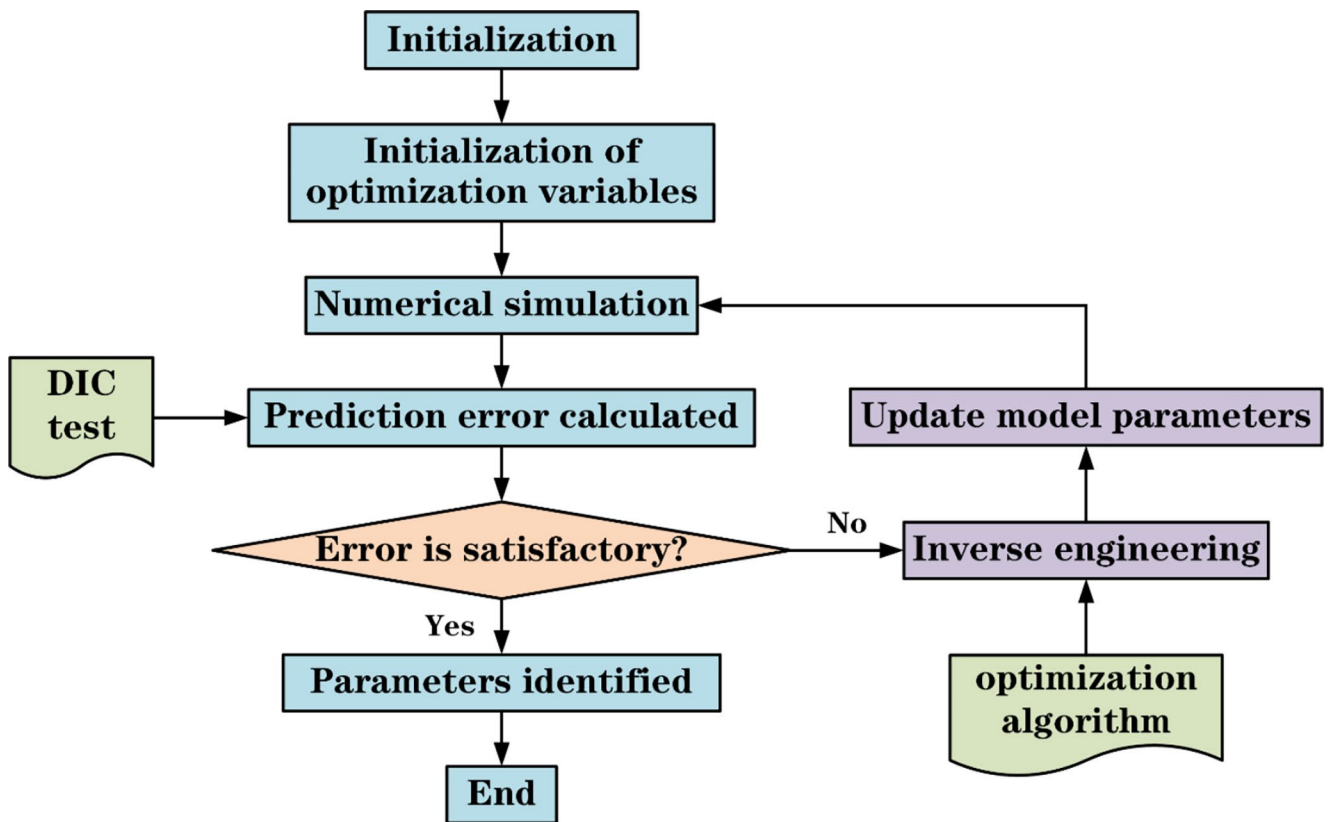

Fig. 6 The iterative process of inverse engineering

simulation by adjusting the parameters of the selected plastic model. Initial guess values are given to the parameters of the constitutive model, and then FE simulations under different experimental conditions are carried out. While adjusting these parameters according to the experimental results, the difference with the numerical calculation results gradually decreases until the optimal parameters are identified. If you want to further confirm the accuracy of the

simulation results, you can compare the estimated local strain field of the sample cross section with the displacement field obtained by the DIC method.

Specifically, the iSight software integrated with the SIMULIA execution engine is used to create a simulation process consisting of a series of automatic FEA simulation, data matching and optimization processes. Several optimization methods are tested for the same task, including gradient descent method, conjugate gradient method, downhill simplex method, and so on. The downhill simplex method with an initial simplex size of 0.1 and a maximum number of iterations of 40 is selected. Different combinations of initial guesses are tested and the results show that the convergence time and convergence value are not significantly affected.

$$err_{notched} = \sum_{i=1}^{n} \left(\frac{F_i^{\exp} - F_i^{\mathrm{num}}}{F_{ave}^{\exp}} \right)^2 \tag{1}$$

where n is the number of samples, $F_i^{\exp}$ and F_i^{num} is the experimental and numerical simulated load values corresponding to the i sample, and $F_{ave}^{\exp}$ is the average load values of the experimental force-stroke curves. Finally, the differences of the calculated results are normalized according to the experimental force to reduce the influence of the different load-bearing capacity according to Eq. (1). The optimization algorithm iterates until the error is less than expected, and the last updated variables are regarded as the optimization parameters of the hardening model.

Identification procedure

The FEMU is applied to inversely identify different phenomenological constitutive models in order to accurately characterize the flow behavior of materials during metal forming [31]. Different models are combined according to the characteristics to describe the strain hardening behavior before and after necking more flexibly [32]. Sung et al. [33] proposed a multiplicative phenomenological constitutive model to accurately describe the strain hardening behavior with temperature under high strain. The accuracy of the model is verified by extensive experiments and simulations that take into account the temperature increase during stretching. Roth and Mohr [34] show that a plastic model with a Johnson–Cook type of rate and temperature-dependency and a combined Swift–Voce strain hardening law can be used to accurately describe the local strain field at large deformations. Recently, Pham et al. [35] introduced the Kim-Tuan hardening model combined with two yield functions to successfully describe the anisotropic plastic behavior of the bulge test. Alternatively, Knysh et al. [13] implemented a cubic function to identify the hardening response before and after necking in a fully coupled manner.

In this study, two typical hardening models are selected to characterize the experimental results of 5182-O aluminum alloy, and the predictions after necking are significantly different according to the structural properties of the respective models. The Swift-Voce model and the p-model are selected to calibrate the hardening curves. As suggested by Sung et al. [33], the hardening curve is fitted by the Swift-Voce model, which is a linear combination of exponential and power model. In addition, the p-model [36] can simulate the hardening behavior before and after necking by flexibly adjusting the value of the parameter p. Then the simulation result after necking is closer to the hardening type of the voce model with a larger value of p. The expressions of the two hardening models and the physical meanings of the related parameters are as follows:

$$\sigma_{eq} = \frac{1}{2} \left[\mathrm{K}\left(\varepsilon_0 + \varepsilon_{pl}^{eq} \right)^{\mathrm{n}} + \left(\mathrm{A} - (\mathrm{A} - \mathrm{B}) \exp\left(-\mathrm{C} \cdot \varepsilon_{pl}^{eq} \right) \right) \right] \tag{2}$$

$$\sigma_{eq} = \begin{cases} \mathrm{K}\left(\varepsilon_{pl}^{eq} + \varepsilon_0 \right)^{\mathrm{n}} & if\ \varepsilon_{pl}^{eq} \leqslant \varepsilon_{\max} \\ \mathrm{K}(\varepsilon_{\max} + \varepsilon_0)^{\mathrm{n}} + \mathrm{Q}\left[1 - e^{-\mathrm{p}\left(\varepsilon_{pl}^{eq} - \varepsilon_{\max} \right)} \right] & if\ \varepsilon_{pl}^{eq} \geqslant \varepsilon_{\max} \end{cases} \tag{3}$$

where σ_{eq} is equivalent stress, $\varepsilon_{\max}$ is maximum uniform strain, the parameters K, ε_0 and n are identified through the available pre-necking data, p is post-necking strain hardening parameter and K, Q, A, B, and C are material constants. As such, the p-model enables a variety of post-necking hardening behaviors to be described whilst retaining the accuracy in the pre-necking region. In order to achieve a smooth transition from pre-necking to post-necking hardening rate in Eq. (3), the relationship between Q and p is derived from the equality of the first derivatives of the two hardening regimes at $\varepsilon_{\max}$.

$$\mathrm{Q} = \frac{\mathrm{K} \cdot \mathrm{n}(\varepsilon_0 + \varepsilon_{\max})^{\mathrm{n}-1}}{\mathrm{p}} \tag{4}$$

Comparison of calibration results of the two models

The local material behavior can be effectively recovered by correcting the force-displacement responses in a single simulation with the FEMU procedure. Therefore, the inverse engineering is extended to modify the properties of the input material during multiple simulations. The first-order solid elements (C3D8R from the ABAQUS library) of the specimen are used with an element edge length of 0.4 mm in the critical region, and the detailed FE meshes is shown in Fig. 7. The FE model has three elements in the thickness of the sheet, and a quarter symmetric model is adopted with symmetric boundary conditions to save running time. The element size sensitivity is studied to balance the
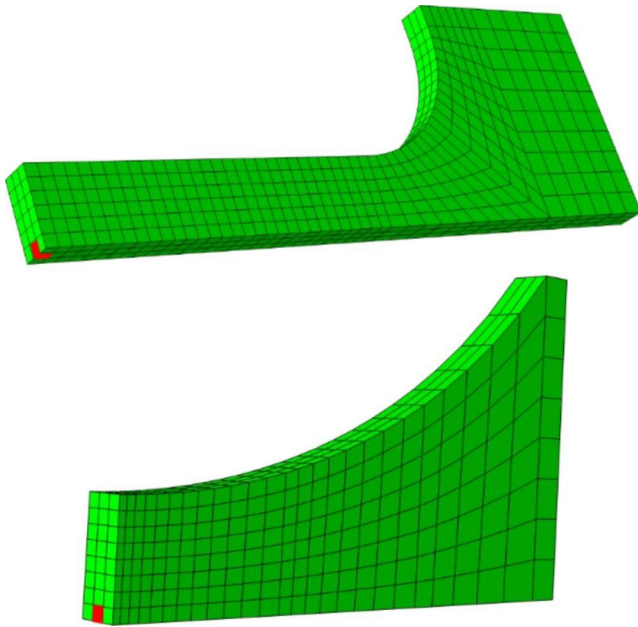
Fig. 7 Detailed solid element meshes of dogbone specimen and notched specimen

requirements of high precision and low computation cost. The reaction force and strain distribution have basically converged when there are 3 elements in the thickness direction. Therefore, a FE model with three elements in the thickness direction is adopted. The inverse FE analysis results calculated by the two hardening models for notched specimen are shown in Fig. 8. It can be seen from the comparison that at relatively low temperatures such as room temperature, the Swift-Voce model is suitable for the uniform strain range. The Swift-Voce model is an ingenious form of transitioning strain hardening from a power-law form to an exponential form. But as the temperature increases, especially at 573 K, the necking phenomenon becomes more prominent. The p-model can easily describe the hardening characteristics at medium strain rates, which fully reflects the advantages of the piecewise function. The Swift hardening law can accurately describe the pre- necking hardening for different temperatures and strain rates. More importantly, the p-model can flexibly describe various hardening behaviors after necking while maintaining the accuracy of the pre- necked region. The p-model can describe different post-necking hardening behaviors by adjusting the parameter p. If p is small, Swift type hardening is retrieved. The larger value of the post-necking hardening parameter p makes the Voce hardening take up a larger proportion and the hardening curve becomes saturated. This above means that the prediction accuracy of the phenomenological hardening model should be evaluated at all hardening stages. Therefore, combining the characteristics of the two representative models,

the hardening model is selected according to the specific calibration results at different temperatures and strain rates.

The flow curves of the two hardening models are extracted from the numerical simulations by the red elements in Fig. 7. They are compared with experimental calculations for dogbone specimens under 24 loading conditions in Fig. 9. It is found that the stress-strain curves of the notched specimen extracted by the FEMU procedure before necking is roughly the same as that calculated by the dogbone specimen. But as the temperature increases, the maximum strain of flow curves calculated by the dogbone specimen becomes smaller. Therefore, extrapolation of pre-necked data to diffuse necking results is completely disordered without the constraints of a well-calibrated hardening model. It becomes very important to calculate and modify the stress-strain curves by the FEMU procedure. The calibration results of the two hardening models need to be evaluated so that the simulated stress-strain curves are much closer to the experimental results than the direct method.

The calibration errors of the two hardening models calculated by Eq. (1) are shown in Fig. 10. It can be found that at low temperature, the calibration results of the two hardening models have little difference by analyzing the error distribution diagram, but the prediction accuracy of the Swift-Voce model is slightly higher than that of the p-model. The calibration accuracy of the p-model is significantly better than that of the Swift-Voce model in the temperature range of 423 to 573 K. Moreover, the Swift-Voce model cannot accurately calibrate the experimental curves with a strain rate of 0.001/s at 523 and 573 K, and the p-model can only calibrate the results up to a strain of 1.0. It shows that it is still very difficult to accurately calibrate the hardening curves under the condition of very early necking at high temperature and low strain rate. In summary, the advantages of the p-model are very obvious especially at a higher temperature than 423 K. Therefore, the Swift-Voce model is finally determined to calibrate the 5 sets of experiments at 300 and 373 K, and the p-model is selected to calibrate the remaining 19 sets of experiments. The parameters of the different models are listed in Appendix A.

Finally, the selected combination is used to characterize the true stress-true strain behavior of the notched specimen. The maximum reliable strains of flow curves identified by inverse engineering approach for the notched specimen tests are compared with the necking strains of the dogbone specimen are shown in Fig. 11. It can be found that the necking strains of the dogbone specimen are roughly distributed between 0.1 and 0.2. However, the strains distribution range of the notched specimen is relatively large, the minimum strain is 0.35 at 373 K with a strain rate of 0.1/s and the maximum strain is 1.69 at 573 K with a strain rate of 0.1/s. Combined with the ratio histogram on the right, it is found
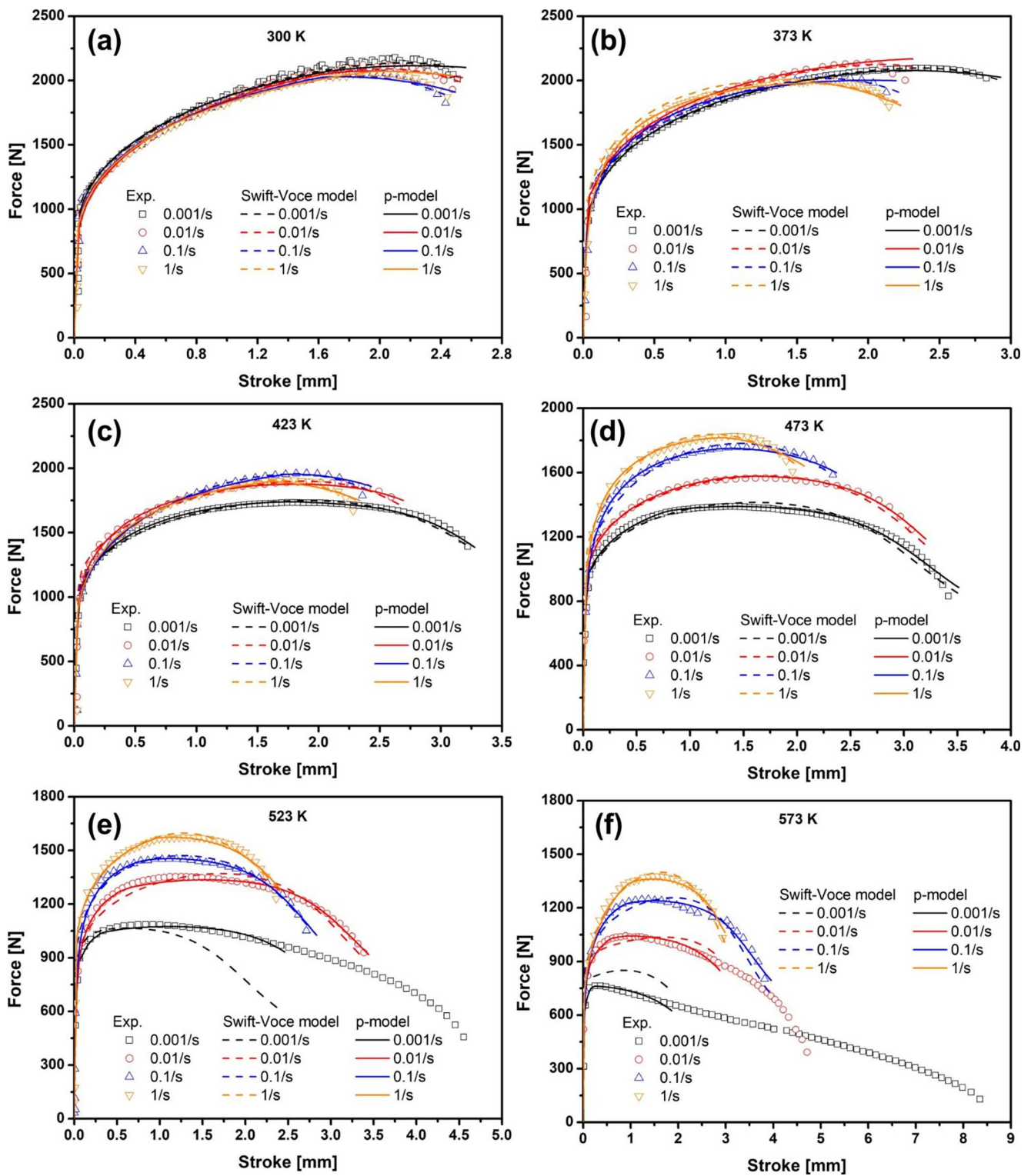
Fig. 8 Calibration results of Swift-Voce model and p-model by inverse engineering method for notched specimens: (a) 300 K, (b) 373 K, (c) 423 K, (d) 473 K, (e) 523 K and (f) 573 K

that the strain ratio of the notched specimen and the dogbone specimen before 423 K is roughly between 1 and 4, but the ratio has a wide range of fluctuations at higher temperatures.

The more prominent ratio reached nearly 60 times at 573 K with a strain rate of 0.001/s. It can be seen that accurate characterization at large strains is of great significance to the
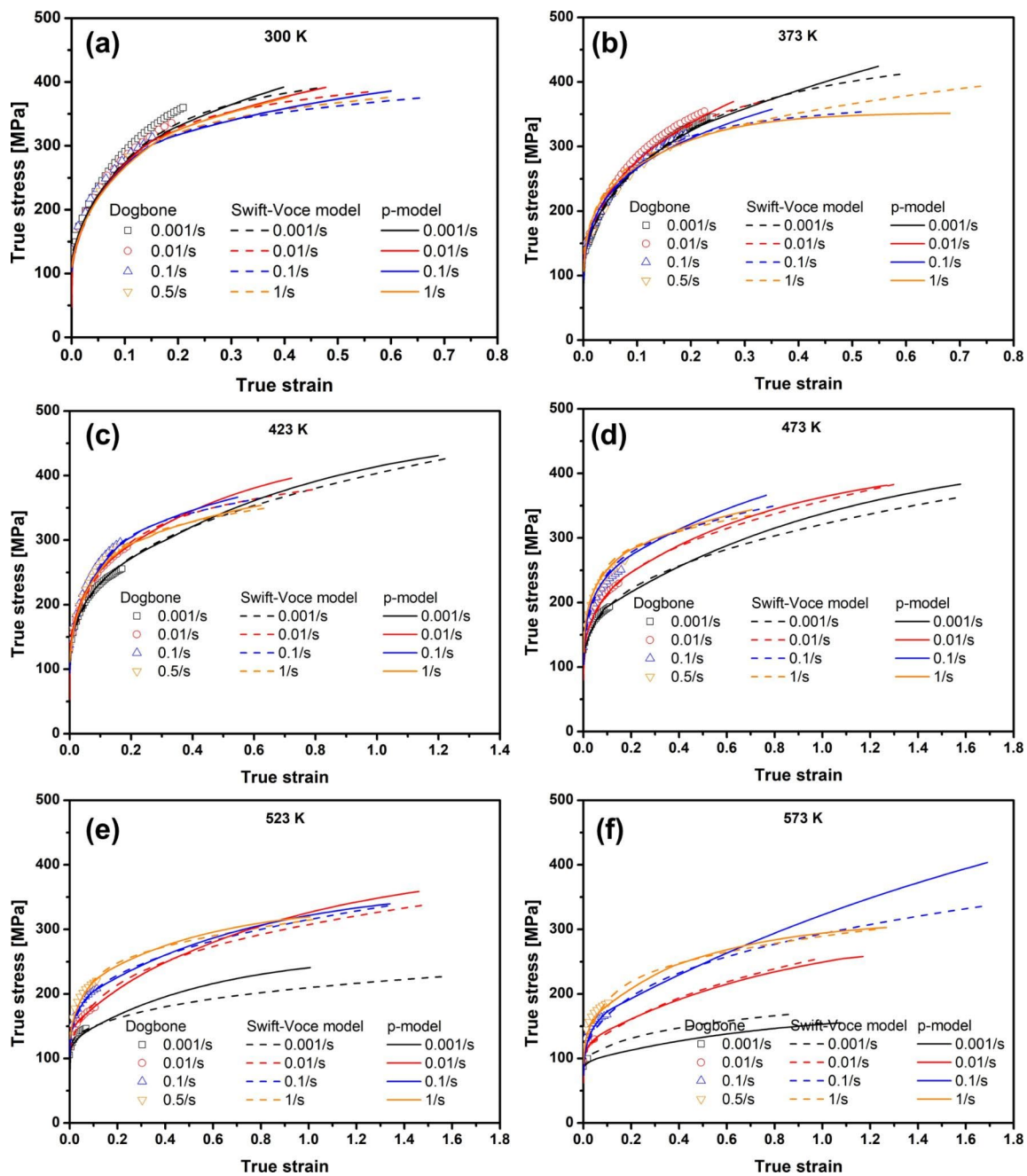
Fig. 9 Comparison of true stress-strain curves of notched specimens extracted by inverse engineering with experimental results of dogbone specimens: (a) 300 K, (b) 373 K, (c) 423 K, (d) 473 K, (e) 523 K and (f) 573 K

reliability of the FE simulation results. The strain in Fig. 11 is generally at the center of the specimen, not on the specimen surface, while the strain as Fig. 5 is the effective surface strain fields measured by DIC at the maximum force of the dogbone and notched specimens for different strain rates of 573 K. So the strain in Fig. 11 is larger than the strain in Fig. 5.

Machine learning

The experimental results show that the mechanical behavior of 5182-O alloy is highly nonlinear. It exhibits negative strain rate sensitivity at low temperature but strong positive strain rate sensitivity at high temperature. However, most traditional constitutive models cannot accurately describe the coupling effect. These models lack flexibility because they have fewer parameters to empirically describe
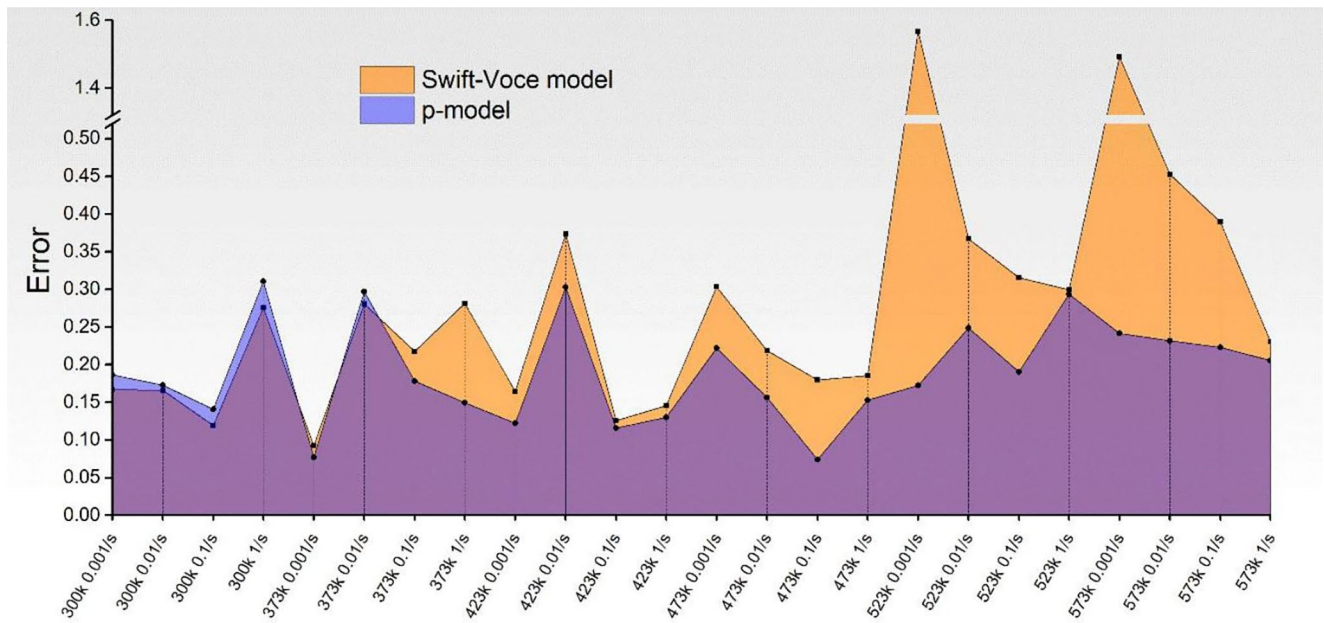
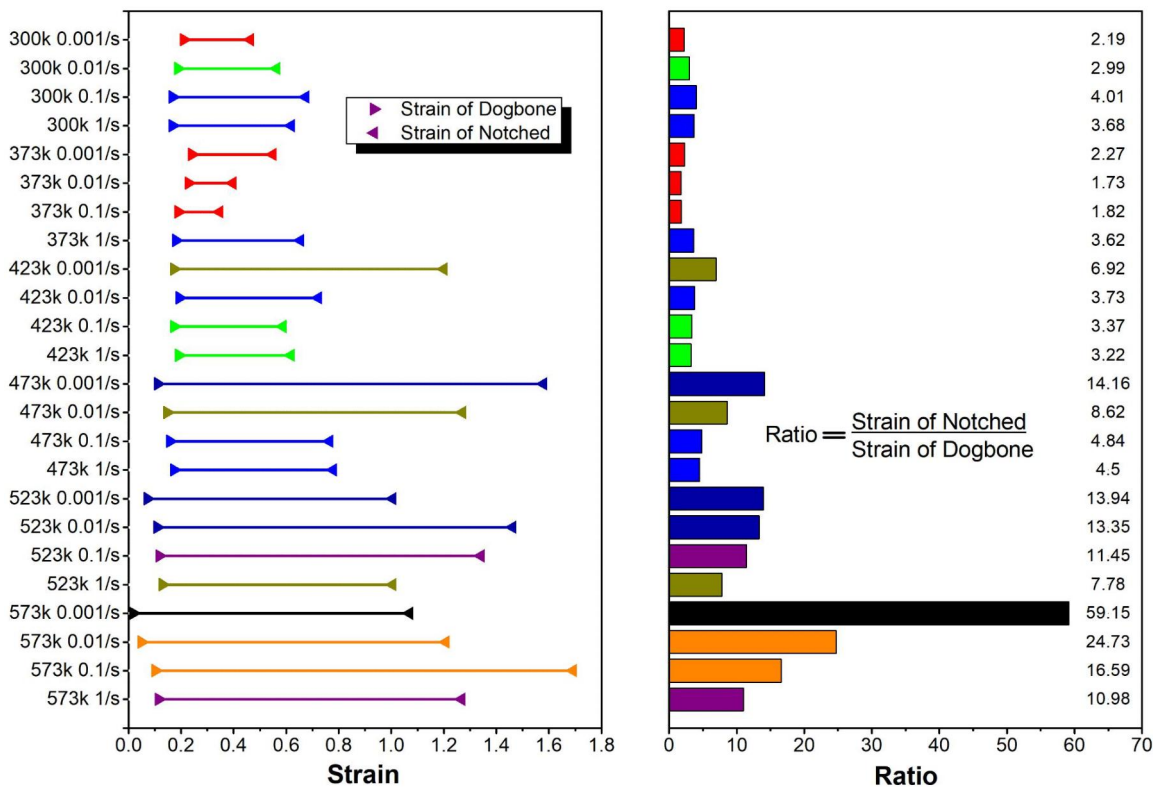**Fig. 10** Comparison of calibration errors of two hardening models

Fig. 11 Comparison of the strain extracted from two specimens

hardening behavior. Therefore, it is the best choice to choose ANN model to analytically describe the coupling effect on the flow curve at large strains.

BP neural network optimized by particle swarm optimization algorithm

Although the back propagation (BP) network has the ability of strong nonlinear mapping, it is easy to obtain local

extreme values and the convergence speed is slow. In order to improve the BP algorithm, the particle swarm optimization algorithm (PSO) is introduced to optimize the initial weights to speed up the convergence of the BP network. The comprehensive PSO-BP network can give full play to the extensive nonlinear mapping ability of BP network and the global search ability of PSO algorithm [37, 38]. The weights and thresholds of the BP neural network are represented by a randomly generated population particle. Each particle corresponds to a fitness value determined by the objective function in order to minimize the prediction error of the neural network. The optimization algorithm flow of PSO-BP network is as follows:

- Step 1. Determination of encoding mode.

The random position and velocity of a particle swarm is initialized and the BP neural network topology is constructed according to the number of input and output parameters.

- Step 2. Fitness function.

$\bar{\sigma}_{pred}$ represents the predicted value corresponding to each experimental value calculated by the trained ANN model. The fitness value of each particle is calculated based on the reciprocal of the mean squared error (MSE).

$$MSE = \frac{1}{N}\sum_{i=1}^{N} (\bar{\sigma}_{exp} - \bar{\sigma}_{pred})^2 \qquad (5)$$

- Step 3. Determination of extremum.

The individual extremum and group extremum of the particles are updated according to the new fitness value. In each iteration, the particle updates its own speed and position through individual extreme values and global extreme values.

- Step 4. Convergence condition.

The weights and thresholds are assigned and saved until the BP network reaches the performance target. P_{best} is the position where each particle's best fitness value is calculated based on its historical motion, and g_{best} is where the best fitness value is calculated for all particles in the global historical motion. The PSO-BP calculation process is summarized in Fig. 12.

Chaotic search process

In order to avoid falling into the local optimum in the early search process, chaos theory and PSO algorithm are used in combination. This chaotic search process can be described as follow:

- Step 1. Initialization of parameters.

The average distance D(t) and fitness variance σ^2 are calculated according to Eqs. (6)-(7) until D(t) <α or σ²<β is satisfied.

$$D(t) = \frac{1}{N \cdot L} \cdot \sum_{i=1}^{N} \sqrt{\sum_{d=1}^{N} (p_{id} - \overline{p_d})^2} \qquad (6)$$

$$\sigma^2 = \sum_{i=1}^{N} \left(\frac{f_i - f_{avg}}{f}\right)^2 \qquad (7)$$

where N represents the population size of particles, L stands for the diagonal maximum length in searching space, D stands for the dimension of the solution space. p_{id} is the dth dimension coordinate value of particle i and $\overline{p_d}$ is the average coordinate value of the dth dimension. The variable f_i represents the fitness value of particle i, f_{avg} is the average fitness value of all particles and f is normalization scale factor.

- Step 2. Perform the chaotic search.

A set of chaotic sequences is generated according to the initialized variable y_0. If chaos iteration n>M, the particles are randomly replaced with the best point. This is then used to verify the end conditions of the PSO process.

Neural network model identification

The stress-strain curves of the notched specimens extracted by the FEMU procedure are used as the input data set for the ANN model describing the coupling effect. There are three inputs: plastic strain, plastic strain rate and temperature. The variables in the input vector $\left[\varepsilon_{pl}^{eq}, \log_{10}(\dot{\varepsilon}), T\right]$ of the neural network correspond to the intervals [0, 0.25], [-3, 0], [298, 573], respectively. The final model structure of strain rate and temperature effect is shown in Fig. 13. In order to achieve the optimal combination between the prediction accuracy and the calculation time of numerical simulation, it is necessary to comprehensively consider the structure and parameters settings of the neural network model [37]. The number of neurons in the first hidden layer has a dominant influence on the prediction accuracy. In addition, too
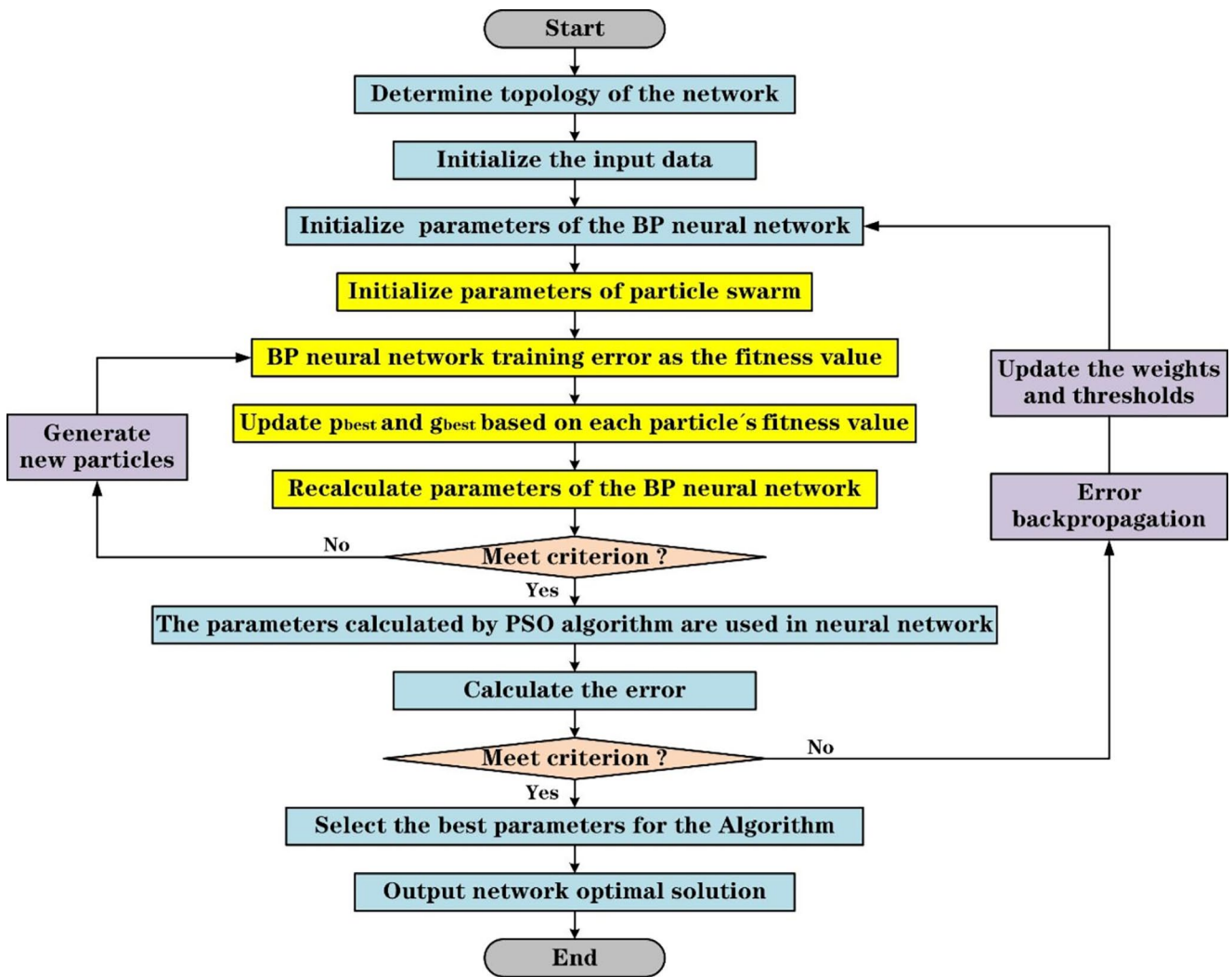
Fig. 12 PSO-BP calculation process

Fig. 13 The structure of ANN model
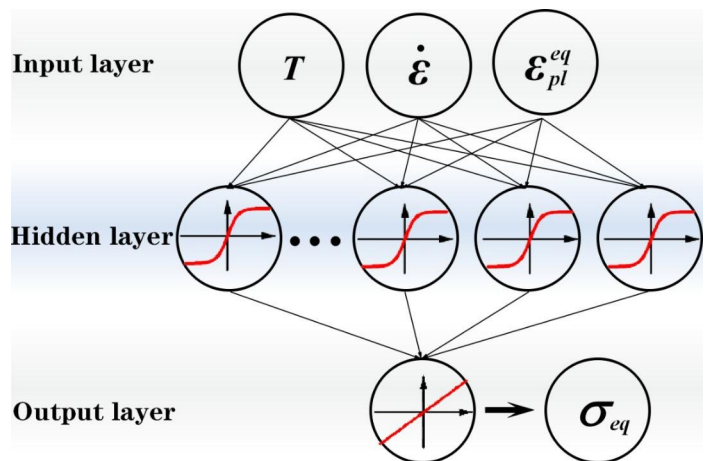
few neurons will lead to the loss of input information, while too many neurons will increase the burden of FE calculation without much effect on improving the accuracy. And the prediction error reaches a plateau after the number of

parameters (the sum of weights and thresholds) reaches a value. The accuracy of prediction does not improve greatly with the further complexity of the network structure, but the calculation time of FE increases proportionally with
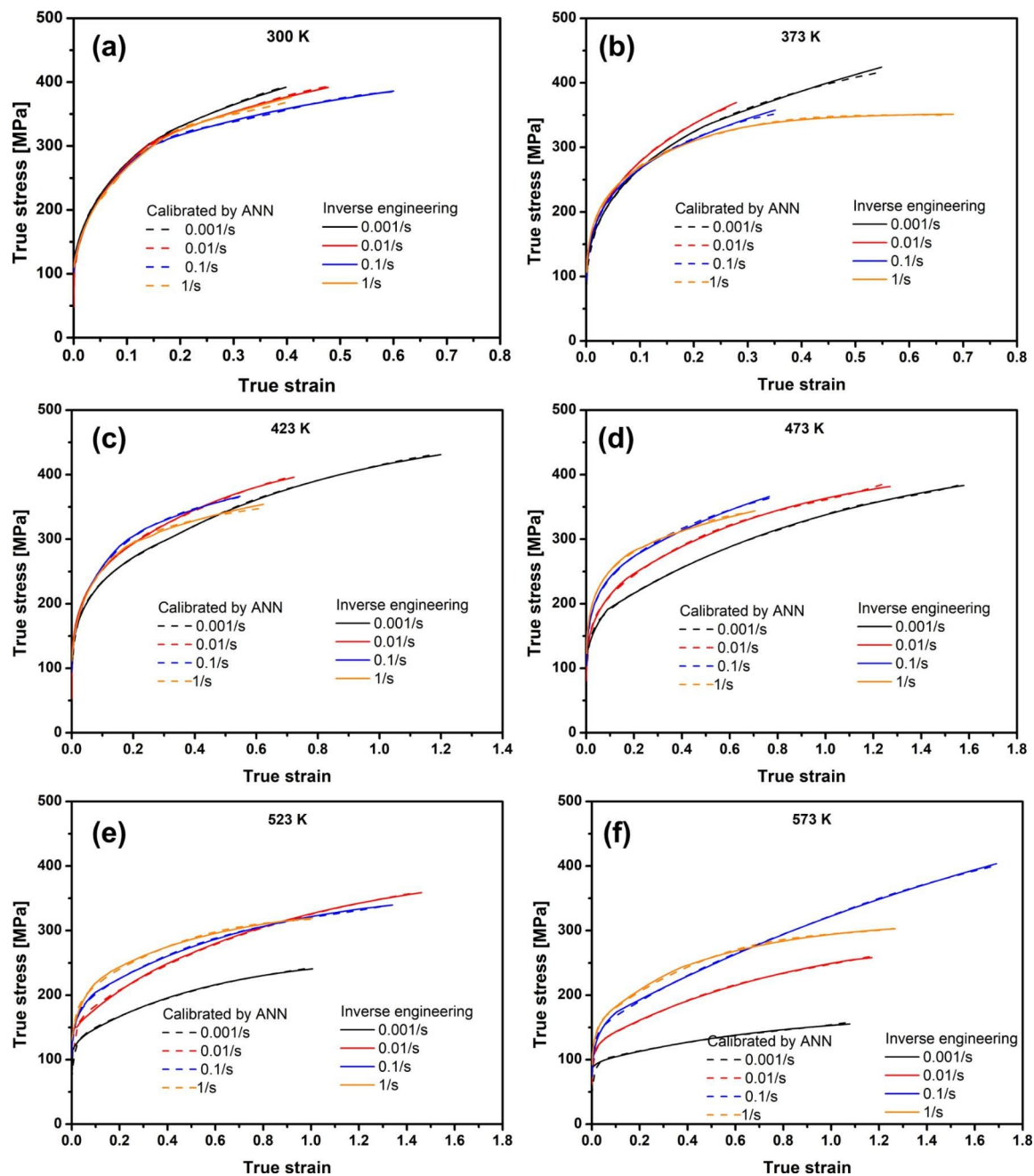
Fig. 14 The stress-strain curves extracted by the FEMU procedure are calibrated by the ANN model: (a) 300 K, (b) 373 K, (c) 423 K, (d) 473 K, (e) 523 K and (f) 573 K

the number of parameters. After the same network structure is optimized by the PSO, the prediction error can quickly reach a low level. Therefore, the PSO-BP network with a single hidden layer of 16 neurons is chosen to fully exploit the potential of high prediction accuracy and low computation time. The tansig (hyperbolic tangent function) is regarded as the activation function of the hidden layer, and purelin (linear function) is regarded as the activation function of the output layer. The best combination of the number of epochs and momentum is 3000 and 0.9, and the learning

rate is adjusted between 0.01 and 0.1 depending on the situation. After the structure and parameters are set, the weights and thresholds are iteratively updated by the Levenberg-Marquardt optimization algorithm. The experimental data are randomly divided into 90% for training and 10% for testing. Therefore, 2413 sets of data are extracted from the FEMU procedure and finally 2172 sets of data are used for the training.

The performance of the above PSO-BP model can be evaluated according to the predicted results in Fig. 14. The
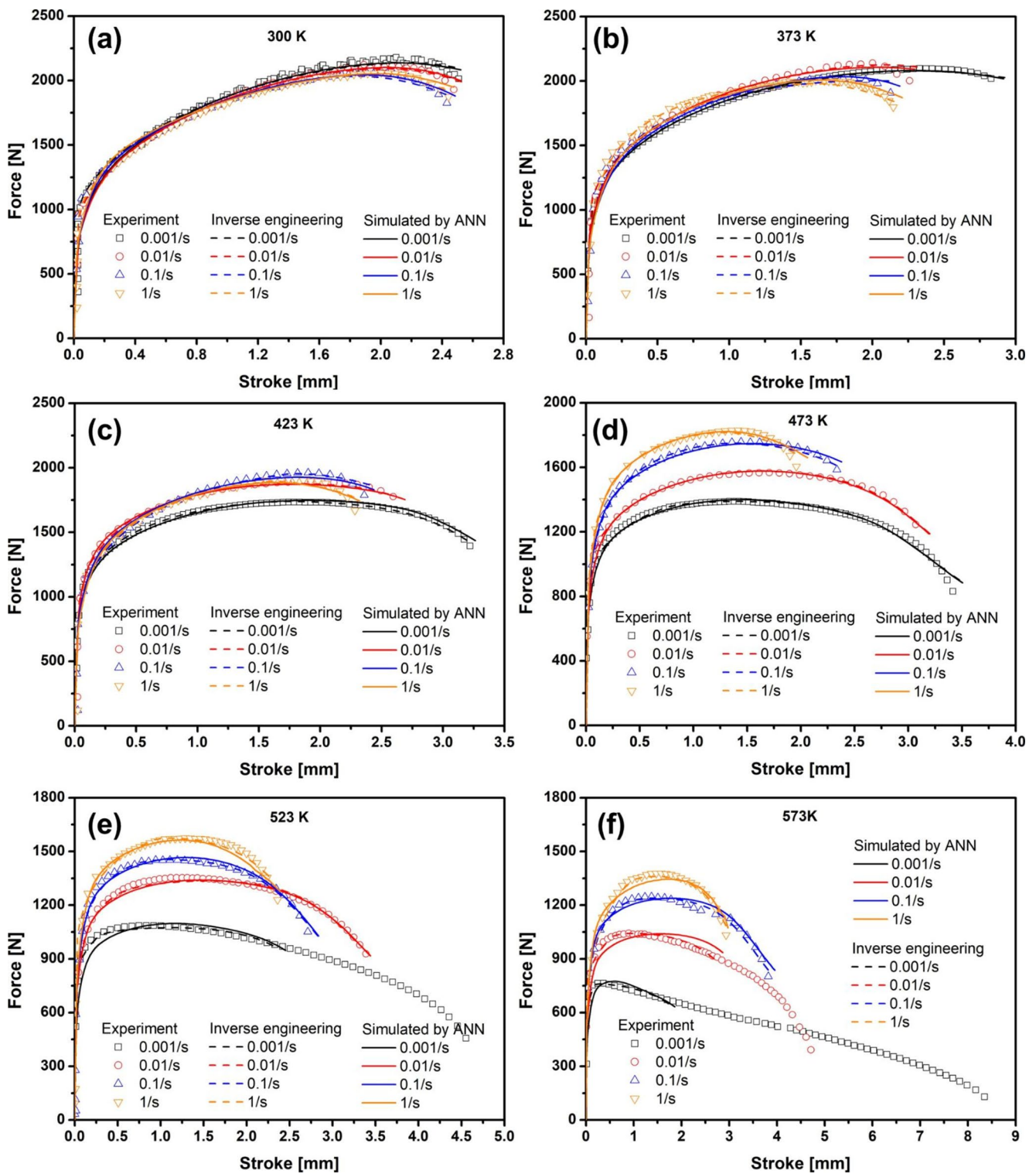
Fig. 15 The FE results of the ANN model are compared with the experimental results and the calibration results by inverse engineering methods of notched specimens at different temperatures and different strain rates: (a) 300 K, (b) 373 K, (c) 423 K, (d) 473 K, (e) 523 K and (f) 573 K

results show that the ANN model can not only correctly calibrate the negative strain rate effect at low temperature. Moreover, it can accurately reflect the positive strain rate effect when the temperature is greater than or equal to

423 K, which becomes more obvious with the increase of temperature. It can reproduce almost all the characteristics at large strains perfectly, such as the fracture strain reaches 1.8 with a strain rate of 0.1/s at 573 K. The ANN model
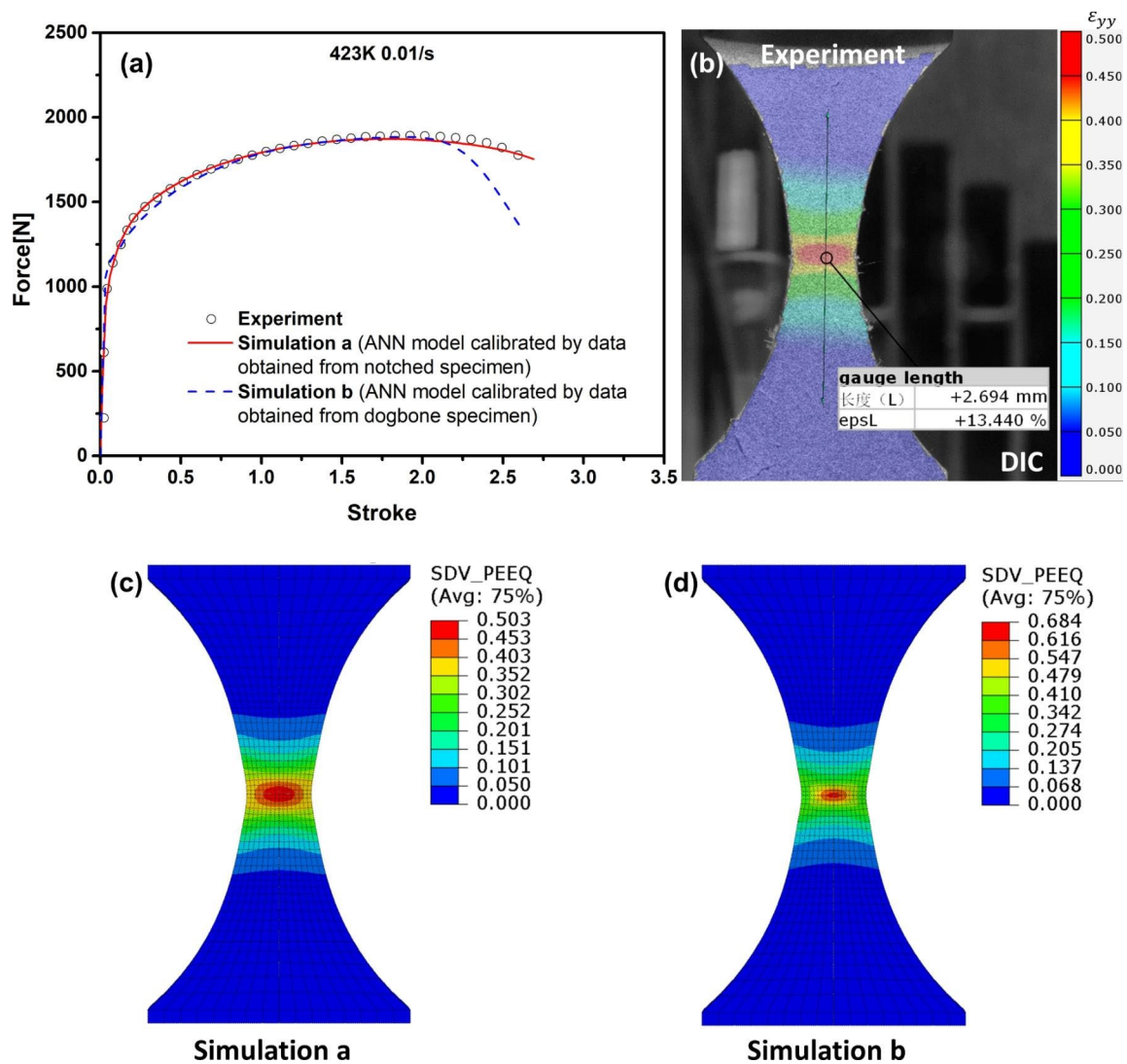
Fig. 16 Experimental and simulation results of notched specimens: (a) the force-displacement curves, (b) the effective strain field calculated by DIC, (c) and (d) the effective strain fields of the ANN model calibrated by data obtained from the notched specimens and the dogbone specimens respectively at the last load step

can also accurately calibrate the high nonlinearity shown by four groups of different strain rates at 523 K. In general, the deformation resistance increases with the equivalent plastic strain at a certain strain rate and temperature. It is worth noting that the curves predicted by the ANN model are still exceptionally smooth despite the large range of training data. In summary, the predictions of ANN model under different temperatures and strain rates have high accuracy compared with experimental data.

Comparison of experimental and numerical simulation results

The calibrated ANN model is embedded into ABAQUS/Explicit to simulate the force-stroke curves of notched specimens. The toolbox of matlab is called to calibrate the experimental data, and then determine the parameters of the ANN model. Finally, these parameters are input into the ANN model implemented in VUMAT of ABAQUS/Explicit written in Fortran. The FE meshes of the quarter symmetric model for inverse engineering and validation are shown in Fig. 7. Different initial temperatures are set and then the temperature remains constant throughout the simulation. The corresponding loading speeds are set according to different strain rates. For all specimens, the displacement history and loading temperature are applicable to all nodes on the FE meshes. The ANN model assumes a von Mises yield surface and isotropic hardening.

The ANN model trained by FEMU procedure is used to predict the tensile force-displacement curves of the notched specimen. The comparison between the FE simulation results and the experimental results under different loading

conditions is shown in Fig. 15. The ANN model can accurately capture the negative strain rate effect of this material at 300 K. Moreover, highly nonlinear dynamic hardening behavior such as positive correlation before 0.1/s strain rate and negative correlation after 0.1/s strain rate at 423 K can also be accurately characterized by the ANN model. The positive strain rate effect becomes more obvious when the test temperature is greater than 473 K. The predictions of the ANN model for the positive strain rate effect at high temperature are in good agreement. Although at high temperatures such as 573 K, the prediction results of the ANN model deviate a little from the inverse results. The rapid necking at high temperature results in the inflection point of necking strain that cannot be predicted very accurately. The comparison results show that the nonlinear coupling effect of thermal softening and strain rate hardening at large strains can be accurately reproduced by the calibrated ANN model.

Another ANN model is trained with the stress-strain curves of the dogbone specimens as the input data set. It is further used to simulate the hardening behavior of notched specimens at different temperatures and strain rates. Figure 16 (a) shows the comparison of the prediction results of the two ANN models with the experimental results at 423 K with a strain rate of 0.01/s. The ANN model calibrated by the data extracted from dogbone specimens at high temperature is found to be only roughly correct in the predicted trend before necking. However, the post-necking prediction is significantly incorrect, and the deformation resistance does not even increase monotonically with the equivalent plastic strain. Figure 16 (b) is the DIC calculations with stroke of 2.694, and Fig. 16 (c) and (d) are the results of the FE simulation of the above two ANN models, respectively. The comparison shows that not only the strain distribution around the local area is close to the predicted value of simulation a, but the equivalent strain value is also very close to the result of simulation a. Therefore, the prediction results of the ANN model calibrated by the data extracted from the dogbone specimens are very different from the experimental results.

Results and discussion

The large strain response of 5182-O aluminium alloy is investigated for uniaxial loading. The effective combination of the inverse engineering method and the ANN model accurately identifies the post-necking hardening response of rate- and temperature-dependent metals. The following conclusions are summarized:

(1) Experiments show that the difference in hardening behavior and fracture strain under different loading conditions is very obvious. The strain rate effect is negative at room temperature, but the strain rate effect becomes positive as the loading temperature increases. Thus, the strain rate and thermal effect is strongly coupled. The displacement of fracture becomes smaller with increasing strain rate at the same temperature. Even as the temperature increases, the necking strain is smaller but the fracture strain is larger.

(2) Suitable constitutive models for different loading conditions are selected in order to obtain higher calibration accuracy as much as possible. The segmented p-model can accurately describe the pre- and post-necking hardening behavior compared to the Swift-Voce model. The FEMU technique is applied during uniaxial tensile testing to inversely identify the post-necking strain hardening behavior.

(3) The appropriate parameters and structure are selected for ANN model in order to ensure the prediction accuracy and the calculation time. The extracted 24 sets of stress-strain are used as the input set to train the ANN model. Finally, the determined ANN model is applied to ABAQUS/Explicit. The method proposed in this paper can accurately predict the large strain response.

(4) It can be found that this method greatly improves the strain range of 5182-O aluminium alloy from the comparison between the strain obtained by the inverse calculation of the notched specimen and the necking strain of the dogbone specimen. Moreover, the FE can almost accurately simulate the large strain behavior of the notched specimen under different loading conditions.

Appendix A. Calibrated parameters of two hardening models

Swift-Voce model							
		K	ε_0	n	A	B	C
300 K	0.001/s	329.22	0.0058	0.3736	536.80	207.16	9.5117
	0.01/s	321.38	0.0044	0.3639	508.96	189.88	11.349
	0.1/s	296.09	0.0093	0.3839	496.86	193.09	13.310
	1/s	357.43	0.0073	0.3300	449.75	171.46	12.587
373 K	0.001/s	464.62	0.0069	0.2738	426.85	146.09	6.5699
	0.01/s	410.64	0.0047	0.3470	468.72	201.30	9.5559
	0.1/s	245.75	0.0296	0.2927	502.22	192.86	11.565
	1/s	604.78	0.0082	0.2680	227.76	109.34	29.467
423 K	0.001/s	529.02	0.0066	0.4110	276.39	194.67	13.007
	0.01/s	324.22	0.0035	0.3531	458.41	241.24	7.5186
	0.1/s	335.81	0.0073	0.3844	448.96	203.29	12.791
	1/s	303.95	0.0085	0.3884	442.91	199.66	15.045

Swift-Voce model

		K	ε_0	n	A	B	C
473 K	0.001/s	422.44	0.0053	0.4000	218.93	175.14	18.458
	0.01/s	416.67	0.0091	0.4483	295.66	214.03	11.151
	0.1/s	367.37	0.0061	0.3915	362.32	207.88	17.840
	1/s	327.20	0.0083	0.3414	378.94	215.46	21.157
523 K	0.001/s	297.24	0.0005	0.2436	122.28	158.73	16.447
	0.01/s	419.12	0.0041	0.3424	195.34	155.24	6.7202
	0.1/s	390.67	0.0046	0.3632	239.01	187.16	28.470
	1/s	308.31	0.0061	0.3370	319.59	205.61	16.095
573 K	0.001/s	246.33	0.00002	0.2587	100.12	144.23	41.066
	0.01/s	425.91	0.0101	0.3829	84.721	145.56	17.087
	0.1/s	390.94	0.0057	0.3844	195.18	152.38	4.7541
	1/s	359.41	0.0011	0.2874	219.27	125.04	12.501

p-model

		K	ε_0	n	ε_{max}	Q	p
300 K	0.001/s	561.40	0.0083	0.3245	0.11	116.67	6.6008
	0.01/s	572.40	0.0061	0.3329	0.11	91.898	8.7197
	0.1/s	560.32	0.0080	0.3312	0.11	76.900	10.077
	1/s	543.01	0.0065	0.3182	0.19	31.664	16.544
373 K	0.001/s	514.87	0.0060	0.2926	0.18	119.04	4.1582
	0.01/s	532.44	0.0070	0.2914	0.24	150.60	2.7750
	0.1/s	451.93	0.0007	0.2295	0.18	135.57	2.8582
	1/s	428.65	0.000004	0.2013	0.20	42.859	7.2813
423 K	0.001/s	388.73	0.0051	0.2256	0.28	351.75	0.6491
	0.01/s	416.17	0.0027	0.2188	0.13	130.86	3.3693
	0.1/s	474.89	0.0042	0.2702	0.15	63.979	7.8474
	1/s	444.06	0.0032	0.2463	0.14	56.294	8.4066
473 K	0.001/s	285.11	0.0011	0.1793	0.12	143.71	1.9774
	0.01/s	308.06	0.0010	0.1643	0.10	182.83	1.8083
	0.1/s	324.20	0.0008	0.1449	0.08	198.70	2.0204
	1/s	325.85	0.0008	0.1313	0.07	183.88	2.1703
523 K	0.001/s	206.12	0.0201	0.1557	0.09	118.85	1.7351
	0.01/s	225.23	0.0026	0.1094	0.05	180.26	1.8348
	0.1/s	277.31	0.0016	0.1412	0.10	125.80	2.1943
	1/s	350.96	0.0087	0.2119	0.04	90.690	8.8691
573 K	0.001/s	129.21	0.0197	0.1005	0.09	72.214	1.2626
	0.01/s	198.88	0.0109	0.1493	0.10	164.01	1.1483
	0.1/s	247.26	0.0059	0.1776	0.09	177.84	1.6027
	1/s	260.77	0.0003	0.1562	0.09	151.42	1.8904

Declarations

Conflict of interest The authors declared that they have no conflicts of interest to this work.

References

1. Miller WS, Zhuang L, Bottema J, Wittebrood AJ, Smet PD, Haszler A, Vieregge A (2000) Recent development in aluminium alloys for the automotive industry. Mater Sci Eng A 280:37–49. https://doi.org/10.1016/S0921-5093(99)00653-X
2. Mansouri LZ, Coër J, Thuillier S, Laurent H, Manach PY (2020) Investigation of Portevin-Le Châtelier effect during Erichsen test. Int J Mater Form 13:687–697. https://doi.org/10.1007/s12289-019-01511-5
3. Kabirian F, Khan AS, Pandey A (2014) Negative to positive strain rate sensitivity in 5xxx series aluminum alloys: Experiment and constitutive modeling. Int J Plast 55:232–246. https://doi.org/10.1016/j.ijplas.2013.11.001
4. Jenab A, Taheri AK (2014) Experimental investigation of the hot deformation behavior of AA7075: Development and comparison of flow localization parameter and dynamic material model processing maps. Int J Mech Sci 78:97–105. https://doi.org/10.1016/j.ijmecsci.2013.11.003
5. Seth M, Vohnout VJ, Daehn GS (2005) Formability of steel sheet in high velocity impact. J Mater Process Technol 168(3):390–400. https://doi.org/10.1016/j.jmatprotec.2004.08.032
6. Khan AS, Baig M (2011) Anisotropic responses, constitutive modeling and the effects of strain-rate and temperature on the formability of an aluminum alloy. Int J Plast 27:522–538. https://doi.org/10.1016/j.ijplas.2010.08.001
7. Abedrabbo N, Pourboghrat F, Carsley J (2007) Forming of AA5182-O and AA5754-O at elevated temperatures using coupled thermo-mechanical finite element models. Int J Plast 23:841–875. https://doi.org/10.1016/j.ijplas.2006.10.005
8. Ge YL, Xia Y, Zhou Q (2022) Influence of pre-straining and heating on strain-rate sensitivity of AA5182-O. Int J Impact Eng 161:104106. https://doi.org/10.1016/j.ijimpeng.2021.104106
9. Sadowski AJ, Rotter JM, Stafford PJ, Reinke T, Ummenhofer T (2017) On the gradient of the yield plateau in structural carbon steels. J Constr Steel Res 130:120–130. https://doi.org/10.1016/j.jcsr.2016.11.024
10. Reis LC, Oliveira MC, Santos AD, Fernandes JV (2016) On the determination of the work hardening curve using the bulge test. Int J Mech Sci 105:158–181. https://doi.org/10.1016/j.ijmecsci.2015.11.009
11. Traphöner H, Clausmeyer T, Tekkaya AE (2021) Methods for measuring large shear strains in in-plane torsion tests. J Mater Process Technol 287:116516. https://doi.org/10.1016/j.jmatprotec.2019.116516
12. Zhang C, Lou YS, Zhang SJ, Clausmeyer T, Tekkaya AE, Fu L, Chen Q, Zhang Q (2021) Large strain flow curve identification for sheet metals under complex stress states. Mech Mater 161:103997. https://doi.org/10.1016/j.mechmat.2021.103997
13. Knysh P, Korkolis YP (2017) Identification of the post-necking hardening response of rate- and temperature-dependent metals. Int J Solids Struct 115–116:149–160. https://doi.org/10.1016/j.ijsolstr.2017.03.012
14. Cordero RR, François M, Lira I, Vial-Edwards C (2005) Whole-field analysis of uniaxial tensile tests by Moiré interferometry. Opt Lasers Eng 43(9):919–936. https://doi.org/10.1016/j.optlaseng.2004.10.002
15. Petit J, Montay G, François M (2014) Strain rate measurements by speckle interferometry for necking investigation in stainless steel. Int J Solids Struct 51(2):540–550. https://doi.org/10.1016/j.ijsolstr.2013.10.029
16. Avril S, Bonnet M, Bretelle AS, Grédiac M, Hild F, Ienny P, Latourte F, Lemosse D, Pagano S, Pagnacco E, Pierron F (2008) Overview of Identification Methods of Mechanical Parameters

Based on Full-field Measurements. Exp Mech 48(4):381. https://doi.org/10.1007/s11340-008-9148-y

17. Yang WK, Wang LY, Song ZM, Luo XM, Zhang GP (2021) Tensile Plasticity of Miniature Specimens for a Low Alloy Steel Investigated by Digital Image Correlation Technique. steel res int 92(7):2000685. https://doi.org/10.1002/srin.202000685

18. Peirs J, Verleysen P, Paepegem WV, Degrieck J (2011) Determining the stress–strain behaviour at large strains from high strain rate tensile and shear experiments. Int J Impact Eng 38(5):406–415. https://doi.org/10.1016/j.ijimpeng.2011.01.004

19. Lou YS, Zhang SJ, Yoon JW (2020) Strength modeling of sheet metals from shear to plane strain tension. Int J Plast 134:102813. https://doi.org/10.1016/j.ijplas.2020.102813

20. Denys K, Coppieters S, Debruyne D (2018) On the identification of a high-resolution multi-linear post-necking strain hardening model. Comptes Rendus Mécanique 346(8):712–723. https://doi.org/10.1016/j.crme.2018.06.002

21. Zhang H, Coppieters S, Jiménez-Peña C, Debruyne D (2019) Inverse identification of the post-necking work hardening behaviour of thick HSS through full-field strain measurements during diffuse necking. Mech Mater 129:361–374. https://doi.org/10.1016/j.mechmat.2018.12.014

22. Jenab A, Sarraf IS, Green DE, Rahmaan T, Worswick MJ (2016) The Use of genetic algorithm and neural network to predict rate-dependent tensile flow behaviour of AA5182-O sheets. Mater Des 94:262–273. https://doi.org/10.1016/j.matdes.2016.01.038

23. Li XY, Roth CC, Mohr D (2019) Machine-learning based temperature- and rate-dependent plasticity model: Application to analysis of fracture experiments on DP steel. Int J Plast 118:320–344. https://doi.org/10.1016/j.ijplas.2019.02.012

24. Jordan B, Gorji MB, Mohr D (2020) Neural network model describing the temperature- and rate-dependent stress-strain response of polypropylene. Int J Plast 135:102811. https://doi.org/10.1016/j.ijplas.2020.102811

25. Lou YS, Huh H (2013) Prediction of ductile fracture for advanced high strength steel with a new criterion: Experiments and simulation. J Mater Process Technol 213(8):1284–1302. https://doi.org/10.1016/j.jmatprotec.2013.03.001

26. Mogucheva A, Yuzbekova D, Kaibyshev R, Lebedkina T, Lebyodkin M (2016) Effect of Grain Refinement on Jerky Flow in an Al-Mg-Sc Alloy. Metall Mater Trans A 47(5):2093–2106. https://doi.org/10.1007/s11661-016-3381-2

27. Zhemchuzhnikova D, Lebyodkin M, Yuzbekova D, Lebedkina T, Mogucheva A, Kaibyshev R (2018) Interrelation between the Portevin Le-Chatelier effect and necking in AlMg alloys. Int J Plast 110:95–109. https://doi.org/10.1016/j.ijplas.2018.06.012

28. Rodriguez P, Srinivasan V (1995) Serrated Plastic Flow Revisited. Solid State Phenom. 42–43: 257–266. https://doi.org/10.4028/www.scientific.net/SSP.42-43.257

29. Mirone G, Barbagallo R (2021) How sensitivity of metals to strain, strain rate and temperature affects necking onset and hardening in dynamic tests. Int J Mech Sci 195:106249. https://doi.org/10.1016/j.ijmecsci.2020.106249

30. Khan AS, Pandey A, Gnäupel-Herold T, Mishra RK (2011) Mechanical response and texture evolution of AZ31 alloy at large strains for different strain rates and temperatures. Int J Plast 27(5):688–706. https://doi.org/10.1016/j.ijplas.2010.08.009

31. Pham QT, Lee BH, Park KC, Kim YS (2018) Influence of the post-necking prediction of hardening law on the theoretical forming limit curve of aluminium sheets. Int J Mech Sci 140:521–536. https://doi.org/10.1016/j.ijmecsci.2018.02.040

32. Mohr D, Marcadet SJ (2015) Micromechanically-motivated phenomenological Hosford–Coulomb model for predicting ductile fracture initiation at low stress triaxialities. Int J Solids Struct 67–68:40–55. https://doi.org/10.1016/j.ijsolstr.2015.02.024

33. Sung JH, Kim JH, Wagoner RH (2010) A plastic constitutive equation incorporating strain, strain-rate, and temperature. Int J Plast 26:1746–1771. https://doi.org/10.1016/j.ijplas.2010.02.005

34. Roth CC, Mohr D (2014) Effect of strain rate on ductile fracture initiation in advanced high strength steel sheets: Experiments and modeling. Int J Plast 56:19–44. https://doi.org/10.1016/j.ijplas.2014.01.003

35. Pham QT, Kim YS (2017) Identification of the plastic deformation characteristics of AL5052-O sheet based on the non-associated flow rule. Met Mater Int 23(2):254–263. https://doi.org/10.1007/s12540-017-6378-5

36. Coppieters S, Kuwabara T (2014) Identification of post-Necking hardening phenomena in ductile sheet metal. Exp Mech 54:1355–1371. https://doi.org/10.1007/s11340-014-9900-4

37. Shang HC, Wu PF, Lou YS, Wang JZ, Chen Q (2022) Machine learning-based modeling of the coupling effect of strain rate and temperature on strain hardening for 5182-O aluminum alloy. J Mater Process Technol 302:117501. https://doi.org/10.1016/j.jmatprotec.2022.117501

38. Ren C, An N, Wang JZ, Li L, Hu B, Shang D (2014) Optimal parameters selection for BP neural network based on particle swarm optimization: A case study of wind speed forecasting. Knowl Based Syst 56:226–239. https://doi.org/10.1016/j.knosys.2013.11.015